Contents lists available at ScienceDirect

Journal of Photochemistry & Photobiology, A: Chemistry

Photodeposition of molybdenum sulfide on MTiO$_3$ (M: Ba, Sr) perovskites for photocatalytic hydrogen evolution

Talha Kuru [a,d], Gizem Yanalak [b], Adem Sarilmaz [c], Emre Aslan [b], Ali Keles [d], Munevver Tuna Genc [a], Faruk Ozel [c,*], Imren Hatay Patir [a,*], Mahmut Kus [e,*], Mustafa Ersoz [f]

[a] Selcuk University, Department of Biotechnology, 42030 Konya, Turkey
[b] Selcuk University, Department of Biochemistry, 42030 Konya, Turkey
[c] Karamanoglu Mehmetbey University, Department of Metallurgical and Materials Engineering, 70200 Karaman, Turkey
[d] GKE Energy R&D Center, 48200 Mugla, Turkey
[e] Konya Technical University, Department of Chemical Engineering, 42075 Konya, Turkey
[f] Selcuk University, Department of Chemistry, 42030 Konya, Turkey

ARTICLE INFO

ABSTRACT

Photocatalytic hydrogen evolution using by semiconductor materials have been studied effectively by converting solar energy into the chemical energy. Perovskite-based materials have been widely used as semiconductor catalysts for the photocatalytic hydrogen production. Herein, molybdenum sulfide photodeposited onto MTiO$_3$ (M: Ba, Sr) perovskites (MTiO$_3$/MoS$_x$) have been investigated on the photocatalytic hydrogen evolution under solar light irradiation in the presence of triethanolamine (TEOA) and eosin Y (EY) as an electron donor and photosensitizer, respectively. Compared to pristine MTiO$_3$, BaTiO$_3$/MoS$_x$ and SrTiO$_3$/MoS$_x$ show a remarkable improvement in the hydrogen production efficiency and stability. Photocatalytic hydrogen evolution activities found in the order of SrTiO$_3$/MoS$_x$ > BaTiO$_3$/MoS$_x$ > MoS$_x$ > SrTiO$_3$ > BaTiO$_3$. In addition, photocatalytic hydrogen activity of SrTiO$_3$/Pt was evaluated for comparison with SrTiO$_3$/MoS$_x$ under the same conditions and SrTiO$_3$/MoS$_x$ produced higher hydrogen activity than SrTiO$_3$/Pt due to the high active sites created by MoS$_x$ on the catalyst surface which is originated from Mo–S and S—S bonds.

1. Introduction

The photocatalytic hydrogen production by sunlight has attracted great attention due to its potential applications in clean energy production. Most of the photo/catalysts are facing with the recombination of electron-hole pairs which is a key factor negatively affect the photocatalytic efficiency. In order to prevent this drawback, researchers have utilized comprehensive techniques on the design of efficient catalysts, such as dye sensitization [1], surface modification [2], noble/non-noble metal deposition [3] or adding co-catalyst [4]. Photocatalytic hydrogen production by using noble-metals increases the cost and also reduces industrial applicability.

SrTiO$_3$ and BaTiO$_3$ perovskite-type oxides can be used as an alternative to mostly used TiO$_2$ because of suitable band positions, optical and crystallographic properties for the efficient photochemical energy conversion reactions [5,6]. These perovskites have been widely used for the photocatalytic hydrogen evolution systems due to their structural

flexibility, suppression of photocorrosion, and physicochemical stability [5]. For example, numerous valuable studies have been recently reported by using different kinds of perovskite based catalysts such as NiO-SrTiO$_3$ [7], BaTiO$_3$/ZnO [8], Rh-doped SrTiO$_3$ [9], g-C$_3$N$_4$ coated SrTiO$_3$ [10], Cr/*N*-codoped SrTiO$_3$ [11], Cu–SrTiO$_3$ [12], TiO$_2$/BaTiO$_3$ [13], BaTiO$_3$/SrTiO$_3$ [14], Co$_3$O$_4$/CdS/SrTiO$_3$ [15], SrTiO$_3$/Bi$_2$S$_3$ [16], Al/BaTiO$_3$ [17], Mo doped BaTiO$_3$ [18], NiS/g-C$_3$N$_4$/SrTiO$_3$ [19], La, Rh-doped SrTiO$_3$ [20]. Co-catalyst free BaTiO$_3$ were investigated for UV-light-driven photocatalytic hydrogen evolution reaction (HER) in Na$_2$S/Na$_2$SO$_4$ electron donor medium [21]. The photocatalytic HER activity of Ag co-catalyst loaded SrTiO$_3$ enhanced 1.25 fold when compared to bare SrTiO$_3$ [22]. The wide band gap catalysts used for photocatalytic water splitting are not suitable for solar driven reactions. In the dye sensitization system, visible light can be captured by dye molecules to produce photogenerated electron/hole pairs and transfer to the conduction band (CB) of the wide band gap semiconductors [23]. Dye-sensitized MgTiO$_3$, CaTiO$_3$ and SrTiO$_3$ perovskite nanocrystals
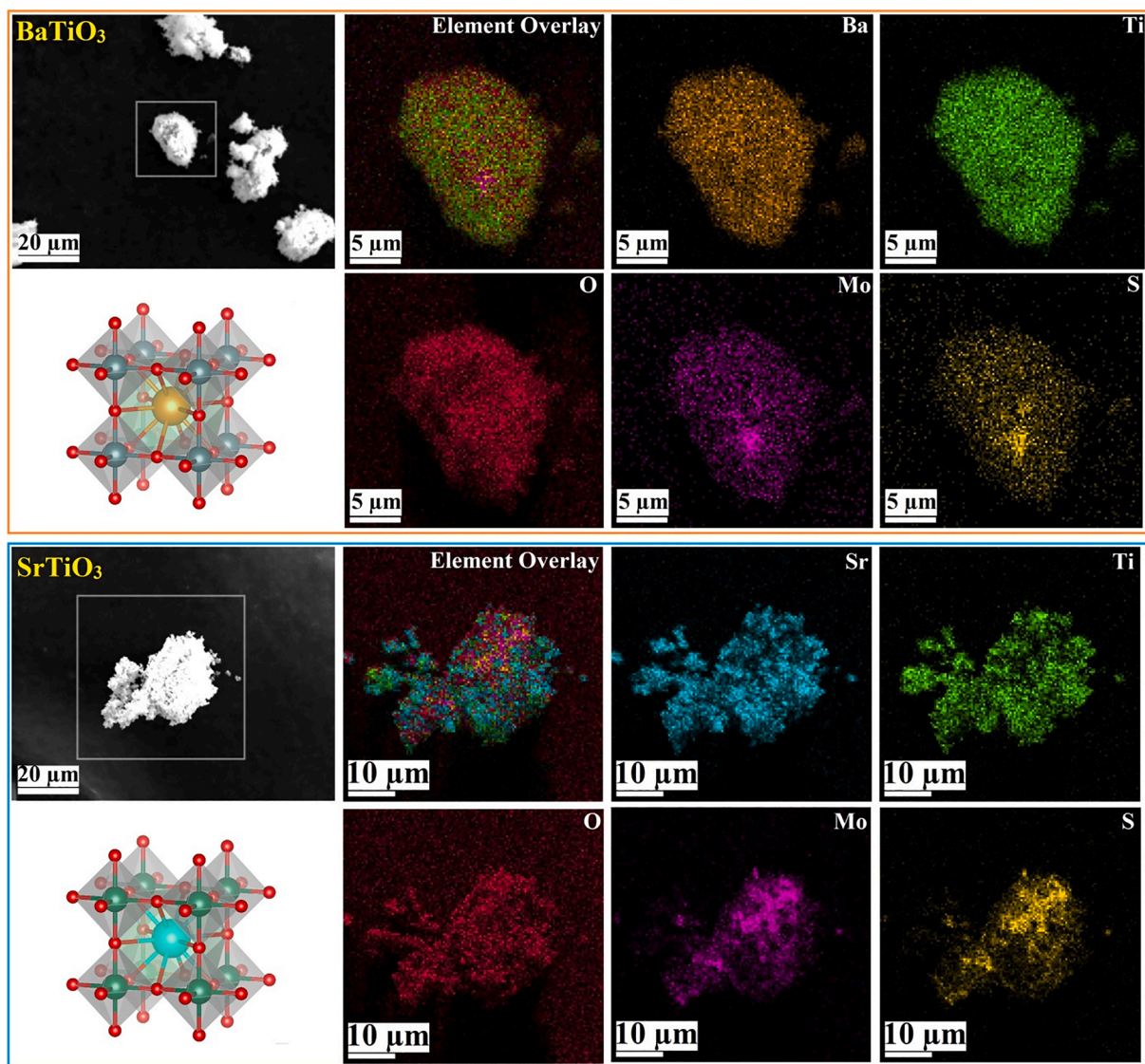

Fig. 1. Elemental MAP images of the photodeposited $BaTiO_3$ and $SrTiO_3$ nanocrystal clusters, respectively.

were investigated for the photocatalytic HER and the highest hydrogen evolution performance was observed by using Ptloaded $SrTiO_3$ [24]. Transition metal dichalcogenides (TMDs) structures are used to improve the catalytic activity by creating active edge sites on the catalyst surface, significantly reducing the charge recombination rate of the catalyst [25–29]. Photocatalytic hydrogen production studies in which it was studied alone with MoS_2 photosensitizer material have been reported, especially TMDs sensitized with Eosin Y produced high photocatalytic hydrogen production [30,31].

In a study using $ZnIn_2S_4$ catalyst, the increase in catalytic activity was discussed when Ni-Mo-S was used as co-catalyst [32]. It was reported that the catalytic activity increased by 5.28 and 2.33 times, respectively, in two different systems with lactic acid and Na_2S/Na_2SO_3. A highly active and cheap co-catalyst MoS_2 is known as an alternative to noble metal Pt for photocatalytic water splitting reactions [33,34]. The catalytic activity of MoS_2 is orginated from the unsaturated S atoms in the edge regions due to the low Gibbs free energy for hydrogen adsorption [35]. The effect of photogenerated MoS_x co-catalyst loaded on $SrTiO_3$ and $BaTiO_3$ have not been reported yet in the literature.

In this study, firstly MoS_x were *in situ* generated on the $MTiO_3$ by reduction of $(NH_4)_2MoS_4$ from excited electrons during the photocatalytic reaction. Then, the effect of the photodeposited MoS_x on $MTiO_3$

(M:Ba, Sr) ($MTiO_3$-MoS_x) were systematically investigated for the photocatalytic HER by using TEOA as a sacrificial electron reagent and EY as a sensitizer. Noteworthily, $MTiO_3$-MoS_x displayed higher photocatalytic activity compared to the pristine $SrTiO_3$, $BaTiO_3$, and MoS_x. $MTiO_3$-MoS_x shows enhanced catalytic performance due to the unsaturated S atoms of the photodeposited MoS_x. The HER activities change in the order of $SrTiO_3/MoS_x > BaTiO_3/MoS_x > MoS_x > SrTiO_3 > BaTiO_3$. $SrTiO_3/MoS_x$ and $BaTiO_3/MoS_x$ display enhanced photocatalytic activity, which increased 18 and 6-fold respectively, as well as show improved stability when compared to pristine $MTiO_3$.

2. Experimental section

2.1. The photocatalytic hydrogen evolution

Before the photocatalytic hydrogen evolution experiments, the pH of the electron donor TEOA solution was adjusted at 9 according to our previous papers with similar catalysts. The whole solutions were bubbled with nitrogen gas in order to remove oxygen [36]. Photochemical Pyrex cell involving the 10 mg catalysts ($SrTiO_3$ and $BaTiO_3$ were commercially obtained from Nanografi), 0.5 mM co-catalyst precursors (($NH_4)_2MoS_4$ or H_2PtCl_6), and 0.33 mM EY in aqueous 20 ml 5 %
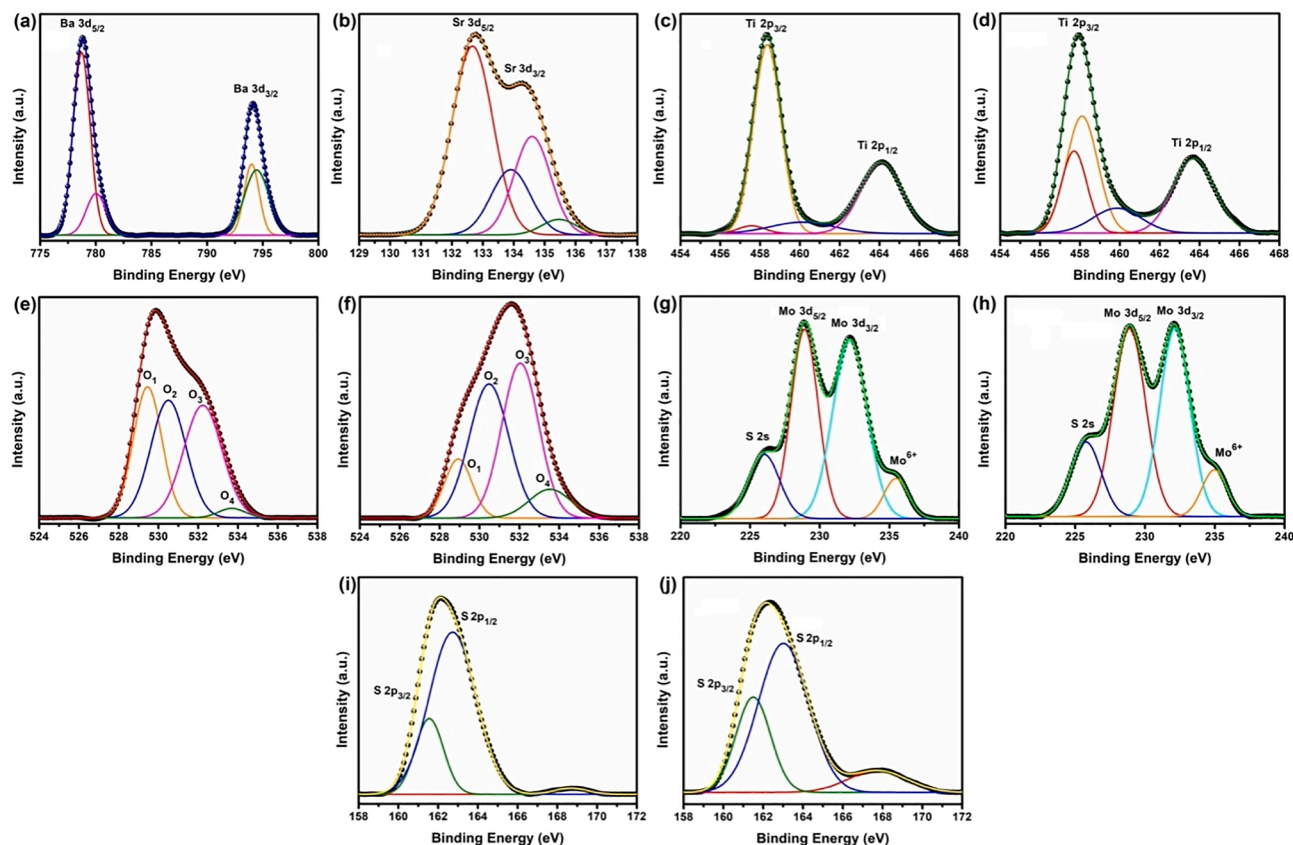
Fig. 2. High resolution XPS spectra of Ba 3d **(a)**, Sr 3d **(b)**, Ti 2p **(c-d)**, O 1 s **(e-f)**, Mo 3d **(g-h)** and S 2p **(i-j)** belonging to BaTiO$_3$-MoS$_x$ **(a-c-e-g-i)** and SrTiO$_3$-MoS$_x$ **(b-d-f-h-j)**.

TEOA solution were combined in the oxygen-free glovebox which are determined in our previous paper with similar oxide materials[37]. The photochemical cell, which was sealed with a silicon rubber septum, was positioned under the solar simulator (300 W) with a fixed distance to obtain 1 sun irradiation intensity measured by a radiometer. The evolved hydrogen was analyzed with a gas chromatography technique (Shimadzu GC-2010 Plus). The solar-to-hydrogen conversion efficiencies (STH) of catalysts were calculated for the photocatalytic HER as follows;

$$STH = \frac{\Delta G^o x R_{H_2}}{P x A} \qquad (1)$$

Where H$_2$ represents the H$_2$ production rate (mmol s^{-1}), ΔG^o the Gibbs free energy of water splitting (237 kJ mol^{-1}), P is the irradiation power density of incident light and, A represents the irradiated area by the incident light (cm^2).

3. Results and discussion

3.1. Characterization of MTiO$_3$ and MTiO$_3$-MoS$_x$ (M: Ba, Sr)

The phase structures and purity of SrTiO$_3$ and BaTiO$_3$ were confirmed by powder X-ray diffraction (XRD) analysis. The XRD analysis results for both nanocrystalline structures were given in **Figure S1**. According to the obtained results, both of the nanocrystals show a cubic crystal structure. The obtained XRD results were compared with ICCD data and were found to be compatible (for BaTiO$_3$; 00-031-0174 and for SrTiO$_3$; 00-035-0734). The unit cell of this polyhedral Ba or Sr centered cubic structure consists of total 9 polyhedral centered on titanium and Ba or Sr. In this structure, each titanium bonds with 6 oxygen atoms, while each Ba or Sr atoms make 12 bonds with O (**Figure S1b**). Also, the

sharp and smooth peaks suggest all of the products being highly crystallized. Moreover, the absence of additional peaks other than the main structure confirms that the perovskites used in the experiments are pure and of high crystallinity.

The surface morphology and further purity of Ba and Sr based perovskite nanocrystals and their MoS$_x$ deposited forms were characterized by scanning electron microscopy (SEM) analysis. The SEM images of the nanocrystals before and after deposition were given in **Figure S2**. From the SEM images, it is clearly seen that the Ba-based perovskites are smaller in size and exhibit a more homogeneous distribution than the Sr-based ones. However, particle agglomeration were seen in the BaTiO$_3$ due to the smaller size of particles, which is originated from increasing surface energy [38,39]. It has been also understood that the partial spaces on the surfaces of the particles were filled with MoS$_x$ after deposition (**Figure S2b and d**). According to the EDX analysis results given in **Figure S2e and f**, it is clearly seen that BaTiO$_3$ and SrTiO$_3$ have approximately the close stochiometric composition. However, due to the homogeneous and smaller size of BaTiO$_3$, higher amount of MoS$_x$ accumulated on BaTiO$_3$ than SrTiO$_3$. Further elemental distribution analyzes of the catalysts were carried out with the SEM-elemental mapping method. As can be clearly seen in **Fig. 1**, the elements that consisted of the particles are clearly visible on the particle clusters. Also, the homogeneous distribution of Mo and S atoms on the particle clusters confirms the SEM and EDX results.

X-ray photoelectron spectroscopy (XPS) analysis has been performed to determine the chemical valance state of elements forming BaTiO$_3$/MoS$_x$ and SrTiO$_3$/MoS$_x$ catalysts. When the high-resolution XPS spectra of Ba 3d are investigated, it is seen that the main peaks centered at 778.8 eV and 794.1 eV correspond to 3d$_{5/2}$ and 3d$_{3/2}$ spin–orbit doublet, respectively (**Fig. 2a**). Further, these peaks have composed of two components ascribed to BaO (778.7 and 794.0 eV) and BaO$_2$ (780.0 and 794.4 eV) [40]. As can be seen in **Fig. 2b**, Sr 3d spectra consist of four
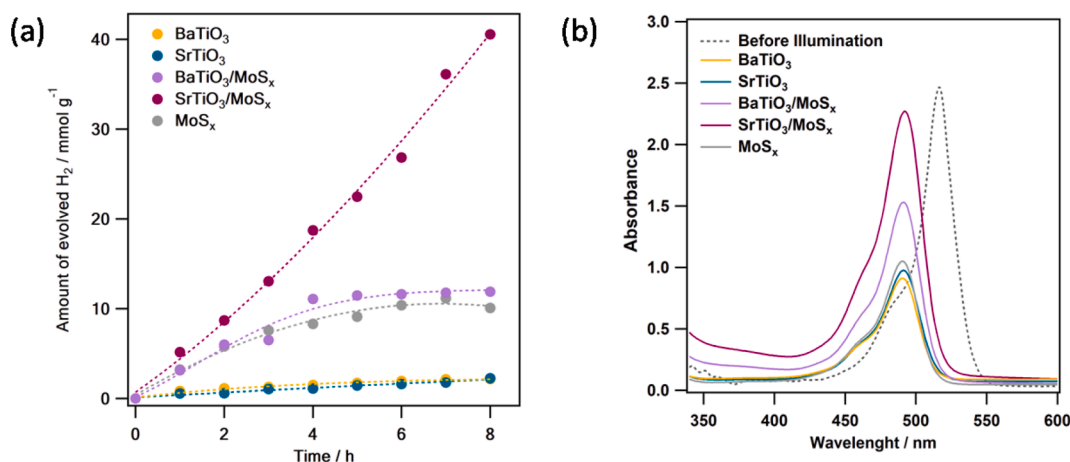
Fig. 3. The comparison results of **(a)** photocatalytic HER performance in TEOA solution with MoS_x, $BaTiO_3$, $SrTiO_3$, $BaTiO_3/MoS_x$ and $SrTiO_3/MoS_x$, **(b)** UV–vis absorption spectrums of reaction solutions before and after 8 h illumination.

components at 132.6, 133.9, 134.6, and 135.55 eV. The peaks at 132.6 and 134.6 eV have been assigned to Sr $3d_{5/2}$ and Sr $3d_{3/2}$, while the peaks at 133.9 and 135.5 eV have been attributed to bonds between strontium and surface impurities [41]. Ti 2p, O 1s, Mo 3d, and S 2p spectra of other common elements forming catalysts show similar characteristic properties. For example, Ti 2p spectra of both materials have formed from two main peaks of spin–orbit doublet consisting of four components (Fig. 2**c-d**).The peaks located at 458.3 and 464 eV correspond to the +4 valance state of titanium, while those at 457.6 and 460.1 eV indicate the existence +3 valance state[42]. The O 1 s spectra were given in Fig. 2**e-f**, and both spectra were fitted with four peaks centered at about 529.0, 530.5, 532.1, and 533.6 eV. The O_1 components at 529.0 eV were assigned to oxygen bonds in the crystal structure. The other peaks belonging to O_2, O_3, and O_4 were ascribed to different oxygen bonds such as H_2O, C–Ti–O, and C–Ti–OH originating from air ambient [43]. Fig. 2**g-h** shows high resolution Mo 3d spectra, and these spectra were fitted by four peaks corresponding to S 2s, Mo $3d_{5/2}$, Mo $3d_{3/2}$, and Mo^{+6} peaks at approximately 225.8, 228.9, 232.1, and 235.3 eV, respectively. The presence of low intensity Mo^{+6} peaks indicate the slight oxidation of molybdenum in the crystal structure. Fig. 2**i-j** is clearly seen that the peaks at 162.1 eV were deconvoluted into $2p_{3/2}$ and $2p_{1/2}$ doublet of S^{2-}. Moreover, the peaks at the higher binding energy (~168.2 eV) demonstrate insufficient oxidation of sulfur atoms [44].

Diffuse reflectance measurements of produced catalysts were carried out to determination of the band gap type and values (**Figure S3a**). The obtained data were used to calculate the absorption of $BaTiO_3$ and $SrTiO_3$ by the Kubelka-Munk equation. The band transition types of the materials were determined as stated in previous studies [45–47], and thus it was confirmed that $BaTiO_3$ has forbidden direct transition and $SrTiO_3$ has allowed direct transition band type. Finally, the energy band diagrams were plotted given in **Figure S3b** according to these results. The band gap values of $BaTiO_3$ and $SrTiO_3$ were estimated from the energy band diagram as 3.23 eV and 3.31 eV, respectively. It has been also measured band gap of EY, which is found as 2.2 eV and in harmony with the literature [48], by using diffuse reflectance spectrum with the same method with $MTiO_3$ (Figure S4).

3.2. Photocatalytic HER activities

The photocatalytic HER by *in situ* photodeposited MoS_x structures on the surface of $MTiO_3$ (M: Ba, Sr) were investigated under visible light by using EY and TEOA as photosensitizer and electron donor, respectively. There is no hydrogen gas was detected without any compounds of the system. Firstly, the photocatalytic HER were performed by using bare $SrTiO_3$ and $BaTiO_3$ and produced hydrogen were found as 2.24 and 2.16

mmol g^{-1}, respectively, under solar light irradiation for 8 h (Fig. 3a). When the effect of MoS_x co-catalyst loading on $MTiO_3$ (M: Ba, Sr) were examined, the HER activities of $BaTiO_3$-MoS_x and $SrTiO_3$-MoS_x were increased about 6 and 18-fold compared to bare $BaTiO_3$ and $SrTiO_3$, respectively. It can be seen that $SrTiO_3/MoS_x$ was shown the highest photocatalytic HER performance as 40.57 mmol g^{-1}, while $BaTiO_3/MoS_x$ was produced 11.88 mmol g^{-1} hydrogen for 8 h of photocatalytic reaction. In order to compare the HER activity of pristine MoS_x with $MTiO_3$ and $MTiO_3$-MoS_x, the photocatalytic activity of only photodeposited MoS_x were investigated and found as 10.07 mmol g^{-1} for 8 h. Photocatalytic hydrogen evolution activities were changed in the order of $SrTiO_3/MoS_x$ > $BaTiO_3/MoS_x$ > MoS_x > $SrTiO_3$ > $BaTiO_3$. In the absence and presence of co-catalyst, $SrTiO_3$ displayed more stable photocatalytic HER activities than $BaTiO_3$ due to aqueous solubility differences, in which $BaTiO_3$ is slightly soluble in the aqueous solutions by leaching of Ba^{2+} species from the surface of $BaTiO_3$ [49]. Insolubility properties of $SrTiO_3$ may be provided the edges for the deposition of co-catalysts. Although the deposition amount of MoS_x on $BaTiO_3$ is more than that of $SrTiO_3$ (as provided from EDX analysis), the higher HER activity and stability is observed with $SrTiO_3/MoS_x$. It can be explained that increasing co-catalyst amount both decreases active site of the catalyst and increases recombination rate due to the aggregate formation [50]. Moreover, the photocatalytic hydrogen production activity of $MTiO_3/MoS_x$ structures were compared with photodepositied $MTiO_3/Pt$ by using photoreduction of H_2PtCl_6. $BaTiO_3/MoS_x$ showed almost the same photocatalytic activity with $BaTiO_3/Pt$. Besides, $SrTiO_3/MoS_x$ displayed more hydrogen production than that of $SrTiO_3/Pt$ (Figure S5). STH efficiencies of $SrTiO_3/MoS_x$, $BaTiO_3/MoS_x$, MoS_x, $SrTiO_3$, $BaTiO_3$ were found out as 13.08, 3.84, 3.25, 0.72, 0.70, respectively. The stabilities of $MTiO_3$ species have been also investigated before and after photocatalytic reactions by XRD analysis. The obtained results were given comparatively in Figure S1**a**. It can be seen from the XRD patterns that no deformation or change occurred in the diffraction peaks after the reaction. These results show that the catalysts used in hydrogen evolution reactions are stable. In the literature, it is crucial to increase the number of active unsaturated S atoms to obtain high HER activity. Also, photodeposited MoS_x on CdS produced higher amount of hydrogen compared to Pt/CdS, which are very promising in terms of finding an alternative to the noble-metal co-catalysts in the previous study [51].

The photostability of species can be explained by the degradation of the EY dye which is determined by UV–vis absorption spectroscopy technique as shown in Fig. 3**b**. Herein, the characteristic peak of EY at 520 nm shifts to 490 nm after visible light illumination, which can be explained by the removal of some bromine atoms from EY [52–54]. In the presence of $BaTiO_3/MoS_x$, $BaTiO_3$, and $SrTiO_3$, the decreased peak
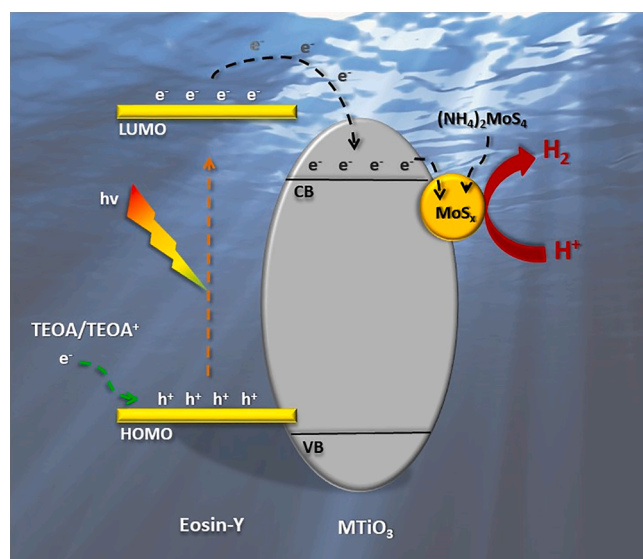
Fig. 4. The proposed photocatalytic HER mechanism for MTiO$_3$/MoS$_x$ catalysts.

intensities are lower than that of SrTiO$_3$/MoS$_x$. These results are in agreement with the hydrogen production rates and stability of MTiO$_3$ and MTiO$_3$/MoS$_x$ [52–54].

Fig. 4 shows the proposed photodeposition and photocatalytic HER mechanism under visible light irradiation. Photogenerated electron-hole pairs are produced in EY under visible light irradiation, then electrons transferred from the LUMO level of EY to the CB of MTiO$_3$. These excited electrons can be used two different reactions, which are (*i*) photo-deposition of co-catalyst precursors on the MTiO$_3$ and also (*ii*) reduction of water to produce hydrogen. For MoS$_x$ photodeposition onto MTiO$_3$ using (NH$_4$)$_2$MoS$_4$ as a precursor, MoS$_4^{-2}$ was reduced to MoS$_x$ by accepting photo-excited electrons from MTiO$_3$. MoS$_x$ provides abundant active sites for photocatalytic hydrogen evolution activity. Also, MoS$_x$ loaded on the perovskite surfaces has abundant unsaturated S atoms which provide strong bonds with H$^+$ in solution, when compared to bridging S$_2^{2-}$ and apical S^{2-} [55]. Photogenerated electrons migrate to MoS$_x$, then protons adsorbed on MoS$_x$ are reduced to hydrogen. As sacrificial agents, TEOA injected the electrons to photogenerated holes, which suppresses the rate of recombination. This reduction reaction provides efficient hydrogen production under visible irradiation.

4. Conclusions

Photocatalytic HER activities of MTiO$_3$ were enhanced by loading MoS$_x$, which is obtained by photodeposition of (NH$_4$)$_2$MoS$_4$ reduction, as a non-noble metal co-catalyst. The HER rates of SrTiO$_3$/MoS$_x$ and BaTiO$_3$/MoS$_x$ were increased approximately 18 and 6-fold, respectively, when compared to their pristine MTiO$_3$ forms. The activity differences between MTiO$_3$ and MTiO$_3$/MoS$_x$ were based on enlarged active sites to occur HER, which is originated from rich in unsaturated S atoms of MoS$_x$. SrTiO$_3$/MoS$_x$ were displayed more hydrogen evolution activity than BaTiO$_3$/MoS$_x$ because of lower amount of photodeposited MoS$_x$ on SrTiO$_3$, which inhibits the aggregation and decreases charge recombination rates. It is also observed that MTiO$_3$/MoS$_x$ shows enhanced and comparable hydrogen production activities than that of MTiO$_3$/Pt. Herein, MoS$_x$ deposition provides the enhanced activity and stability during the photocatalytic reaction, which gives new hope for the use of non-noble metal co-catalyst in perovskites. MTiO$_3$/MoS$_x$ perovskites favors to in-depth understanding for photo/catalysis and also paves the way for current and future research for the design of perovskite materials to improve their photo/catalytic performance and stability.

CRediT authorship contribution statement

Talha Kuru: Formal analysis, Writing – original draft. **Gizem Yanalak:** Formal analysis, Writing – original draft. **Adem Sarilmaz:** Formal analysis, Writing – original draft. **Emre Aslan:** Writing – review & editing, Supervision. **Ali Keleş:** Formal analysis. **Munevver Tuna Genc:** Formal analysis. **Faruk Ozel:** Writing – review & editing, Supervision. **Imren Hatay Patir:** Writing – review & editing, Supervision. **Mahmut Kus:** Supervision. **Mustafa Ersoz:** Supervision.

Declaration of Competing Interest

The authors declare that they have no known competing financial interests or personal relationships that could have appeared to influence the work reported in this paper.

Data availability

No data was used for the research described in the article.

Appendix A. Supplementary data

Supplementary data to this article can be found online at https://doi.org/10.1016/j.jphotochem.2022.114375.

References

[1] W. Zhang, Y. Li, X. Zeng, S. Peng, Synergetic effect of metal nickel and graphene as a cocatalyst for enhanced photocatalytic hydrogen evolution via dye sensitization, Sci. Rep. 5 (2015) 10589.

[2] Q. Xiang, F. Li, D. Zhang, Y. Liao, H. Zhou, Plasma-based surface modification of g-C$_3$N$_4$ nanosheets for highly efficient photocatalytic hydrogen evolution, Appl. Surf. Sci. 495 (2019), 143520.

[3] R. Kavitha, P.M. Nithya, S. Girish Kumar, Noble metal deposited graphitic carbon nitride based heterojunction photocatalysts, Appl. Surf. Sci. 508 (2020), 145142.

[4] Y. Li, H. Li, Y. Li, S. Peng, Y.H. Hu, Fe-B alloy coupled with Fe clusters as an efficient cocatalyst for photocatalytic hydrogen evolution, Chem. Eng. J. 344 (2018) 506–513.

[5] M. Ganapathy, Y. Hsu, J. Thomas, C.T. Chang, V.J.J.o.M.S. Alagan, Co-catalyst free SrTiO$_3$ nano-cube for efficient photocatalytic hydrogen production, (2021) 1-13.

[6] T. Chen, J. Meng, S. Wu, J. Pei, Q. Lin, X. Wei, J. Li, Z. Zhang, Room temperature synthesized BaTiO$_3$ for photocatalytic hydrogen evolution, J. Alloys Compd. 754 (2018) 184–189.

[7] Y. Fo, Y. Wang, Y. Ma, H. Dong, X. Zhou, Origin of highly efficient photocatalyst NiO/SrTiO$_3$ for overall water splitting: Insights from density functional theory calculations, J. Solid State Chem. 292 (2020), 121683.

[8] X. Zhou, S. Wu, C. Li, F. Yan, H. Bai, B. Shen, H. Zeng, J. Zhai, Piezophototronic effect in enhancing charge carrier separation and transfer in ZnO/BaTiO$_3$ heterostructures for high-efficiency catalytic oxidation, Nano Energy 66 (2019), 104127.

[9] M.G.C. Zoontjes, K. Han, M. Huijben, W.G. van der Wiel, G. Mul, The effect of Rhδ + dopant in SrTiO$_3$ on the active oxidation state of co-catalytic Pt nanoparticles in overall water splitting, Catal. Sci. Technol. 6 (2016) 7793–7799.

[10] X. Xu, G. Liu, C. Randorn, J.T.S. Irvine, g-C$_3$N$_4$ coated SrTiO$_3$ as an efficient photocatalyst for H$_2$ production in aqueous solution under visible light irradiation, Int. J. Hydrogen Energy 36 (2011) 13501–13507.

[11] H. Yu, S. Yan, Z. Li, T. Yu, Z. Zou, Efficient visible-light-driven photocatalytic H$_2$ production over Cr/N-codoped SrTiO$_3$, Int. J. Hydrogen Energy 37 (2012) 12120–12127.

[12] D.-N. Bui, J. Mu, L. Wang, S.-Z. Kang, X. Li, Preparation of Cu-loaded SrTiO$_3$ nanoparticles and their photocatalytic activity for hydrogen evolution from methanol aqueous solution, Appl. Surf. Sci. 274 (2013) 328–333.

[13] H. Li, Y. Song, J. Zhang, J. He, Turbulence enhanced ferroelectric-nanocrystal-based photocatalysis in urchin-like TiO$_2$/BaTiO$_3$ microspheres for hydrogen evolution, Nanoscale Adv. 3 (2021) 5618–5625.

[14] X. Liu, X. Shen, B. Sa, Y. Zhang, X. Li, H. Xue, Piezotronic-enhanced photocatalytic performance of heterostructured BaTiO$_3$/SrTiO$_3$ nanofibers, Nano Energy 89 (2021), 106391.

[15] Z. Chen, J. Pan, J. Mei, Q. Yu, P. Wang, P. Wang, J. Wang, C. Song, Y. Zheng, C. Li, Ternary Co$_3$O$_4$/CdS/SrTiO$_3$ core-shell pn junctions toward enhanced

photocatalytic hydrogen production activity, J. Environ. Chem. Eng. 9 (2021), 104895.

[16] M. Ganapathy, Y. Hsu, J. Thomas, L.-Y. Chen, C.-T. Chang, V. Alagan, Preparation of SrTiO$_3$/Bi$_2$S$_3$ heterojunction for efficient photocatalytic hydrogen production, Energy Fuels 35 (2021) 14995–15004.

[17] L. Guo, C. Zhong, J. Cao, Y. Hao, M. Lei, K. Bi, Q. Sun, Z.L. Wang, Enhanced photocatalytic H$_2$ evolution by plasmonic and piezotronic effects based on periodic Al/BaTiO$_3$ heterostructures, Nano Energy 62 (2019) 513–520.

[18] P. Xie, F. Yang, R. Li, C. Ai, C. Lin, S. Lin, Improving hydrogen evolution activity of perovskite BaTiO$_3$ with Mo doping: experiments and first-principles analysis, Int. J. Hydrogen Energy 44 (2019) 11695–11704.

[19] X.-L. Luo, G.-L. He, Y.-P. Fang, Y.-H. Xu, Nickel sulfide/graphitic carbon nitride/strontium titanate (NiS/g-C$_3$N$_4$/SrTiO$_3$) composites with significantly enhanced photocatalytic hydrogen production activity, J. Colloid Interface Sci. 518 (2018) 184–191.

[20] Y. Kageshima, T. Kawanishi, D. Saeki, K. Teshima, K. Domen, H. Nishikiori, Boosted hydrogen-evolution kinetics over particulate lanthanum and rhodium-doped strontium titanate photocatalysts modified with phosphonate groups, Angew. Chem. Int. Ed. 60 (2021) 3654–3660.

[21] K. Karthik, C.V. Reddy, K.R. Reddy, R. Ravishankar, G. Sanjeev, R.V. Kulkarni, N. P. Shetti, A. Raghu, Barium titanate nanostructures for photocatalytic hydrogen generation and photodegradation of chemical pollutants, J. Mater. Sci.: Mater. Electron. 30 (2019) 20646–20653.

[22] J.E. Ramos-Sanchez, R. Camposeco, S.-W. Lee, V. Rodriguez-Gonzalez, Sustainable synthesis of AgNPs/strontium-titanate-perovskite-like catalysts for the photocatalytic production of hydrogen, Catal. Today 341 (2020) 112–119.

[23] P. Chowdhury, G. Malekshoar, A.K. Ray, Dye-sensitized photocatalytic water splitting and sacrificial hydrogen generation: current status and future prospects, Inorganics 5 (2017) 34.

[24] T. Puangpetch, P. Sommakettarin, S. Chavadej, T. Sreethawong, Hydrogen production from water splitting over Eosin Y-sensitized mesoporous-assembled perovskite titanate nanocrystal photocatalysts under visible light irradiation, Int. J. Hydrogen Energy 35 (2010) 12428–12442.

[25] L. Xie, L. Wang, W. Zhao, S. Liu, W. Huang, Q. Zhao, WS2 moiré superlattices derived from mechanical flexibility for hydrogen evolution reaction, Nat. Commun. 12 (2021) 1–9.

[26] L. Wang, L. Xie, W. Zhao, S. Liu, Q. Zhao, Oxygen-facilitated dynamic active-site generation on strained MoS2 during photo-catalytic hydrogen evolution, Chem. Eng. J. 405 (2021), 127028.

[27] S. Wang, L. Wang, L. Xie, W. Zhao, X. Liu, Z. Zhuang, Y. Zhuang, J. Chen, S. Liu, Q. Zhao, Dislocation-strained MoS2 nanosheets for high-efficiency hydrogen evolution reaction, Nano Res. (2022) 1–8.

[28] X. Liu, Y. Hou, M. Tang, L. Wang, Atom elimination strategy for MoS$_2$ nanosheets to enhance photocatalytic hydrogen evolution, Chin. Chem. Lett. (2022).

[29] C. Sun, L. Wang, W. Zhao, L. Xie, J. Wang, J. Li, B. Li, S. Liu, Z. Zhuang, Q. Zhao, Atomic-level design of active site on two-dimensional MoS toward efficient hydrogen evolution: experiment, theory, and artificial intelligence modelling, Adv. Funct. Mater. (2022) 2206163.

[30] X. Cheng, L. Wang, L. Xie, C. Sun, W. Zhao, X. Liu, Z. Zhuang, S. Liu, Q. Zhao, Defect-driven selective oxidation of MoS2 nanosheets with photothermal effect for Photo-Catalytic hydrogen evolution reaction, Chem. Eng. J. 439 (2022), 135757.

[31] M. Liu, H. Li, S. Liu, L. Wang, L. Xie, Z. Zhuang, C. Sun, J. Wang, M. Tang, S. Sun, Tailoring activation sites of metastable distorted 1T'-phase MoS2 by Ni doping for enhanced hydrogen evolution, Nano Res. (2022) 1–7.

[32] J. Chen, Y. Tang, S. Wang, L. Xie, C. Chang, X. Cheng, M. Liu, L. Wang, L. Wang, Ingeniously designed Ni-Mo-S/ZnIn$_2$S$_4$ composite for multi-photocatalytic reaction systems, Chin. Chem. Lett. 33 (2022) 1468–1474.

[33] Y. Yang, Y. Zhang, Z. Fang, L. Zhang, Z. Zheng, Z. Wang, W. Feng, S. Weng, S. Zhang, P. Liu, Simultaneous realization of enhanced photoactivity and promoted photostability by multilayered MoS2 coating on CdS nanowire structure via compact coating methodology, ACS Appl. Mater. Interfaces 9 (2017) 6950–6958.

[34] X. Zong, H. Yan, G. Wu, G. Ma, F. Wen, L. Wang, C. Li, Enhancement of photocatalytic H$_2$ evolution on CdS by loading MoS$_2$ as cocatalyst under visible light irradiation, J. Am. Chem. Soc. 130 (2008) 7176–7177.

[35] B. Hinnemann, P.G. Moses, J. Bonde, K.P. Jørgensen, J.H. Nielsen, S. Horch, I. Chorkendorff, J.K. Nørskov, Biomimetic hydrogen evolution: MoS$_2$ nanoparticles as catalyst for hydrogen evolution, J. Am. Chem. Soc. 127 (2005) 5308–5309.

[36] X. Ma, Y. Liu, Y. Wang, Z. Jin, Amorphous CoS x Growth on CaTiO$_3$ Nanocubes formed S-Scheme heterojunction for photocatalytic hydrogen production, Energy Fuels 35 (2021) 6231–6239.

[37] E. Aslan, E. Genc, M. Ozmen, I.H. Patir, M. Ersoz, In situ grown molybdenum sulfide on Laponite D clay: Visible-light-driven hydrogen evolution for high solar-to-hydrogen (STH) efficiencies, J. Photochem. Photobiol., A 419 (2021), 113469.

[38] M. Platt, R.A. Dryfe, E.P. Roberts, Controlled deposition of nanoparticles at the liquid–liquid interface, Chem. Commun. (2002) 2324–2325.

[39] M. Platt, R.A. Dryfe, Structural and electrochemical characterisation of Pt and Pd nanoparticles electrodeposited at the liquid/liquid interface: Part 2, PCCP 7 (2005) 1807–1814.

[40] I. Spasojevic, G. Sauthier, J.M. Caicedo, A. Verdaguer, N. Domingo, Oxidation processes at the surface of BaTiO$_3$ thin films under environmental conditions, Appl. Surf. Sci. 565 (2021), 150288.

[41] J.-Y. Baek, S.Y. Lee, H. Seo, Aluminum doping for optimization of ultrathin and high-k dielectric layer based on SrTiO$_3$, J. Mater. Sci. Technol. 42 (2020) 28–37.

[42] B. Bharti, S. Kumar, H.-N. Lee, R. Kumar, Formation of oxygen vacancies and Ti3+ state in TiO2 thin film and enhanced optical properties by air plasma treatment, Sci. Rep. 6 (2016) 1–12.

[43] V. Natu, M. Benchakar, C. Canaff, A. Habrioux, S. Celerier, M.W. Barsoum, A critical analysis of the X-ray photoelectron spectra of Ti3C2Tz MXenes, Matter 4 (2021) 1224–1251.

[44] B. Li, L. Jiang, X. Li, P. Ran, P. Zuo, A. Wang, L. Qu, Y. Zhao, Z. Cheng, Y. Lu, Preparation of monolayer MoS2 quantum dots using temporally shaped femtosecond laser ablation of bulk MoS2 targets in water, Sci. Rep. 7 (2017) 1–12.

[45] A. Sarilmaz, G. Yanalak, E. Aslan, F. Ozel, I.H. Patir, M. Ersoz, Shape-controlled synthesis of copper based multinary sulfide catalysts for enhanced photocatalytic hydrogen evolution, Renewable Energy 164 (2021) 254–259.

[46] T.L. Le, S. Guillemet-Fritsch, P. Dufour, C. Tenailleau, Microstructural and optical properties of spinel oxide MxCo2− xMnO4 (M= Ni, Zn or Cu; 0< x< 1) thin films prepared by inorganic polycondensation and dip-coating methods, Thin Solid Films 612 (2016) 14–21.

[47] M. Borah, D. Mohanta, Structural and optoelectronic properties of Eu2+-doped nanoscale barium titanates of pseudo-cubic form, J. Appl. Phys. 112 (2012), 124321.

[48] R. Sharma, A. Kamal, R.K. Mahajan, Detailed study of interactions between eosin yellow and gemini pyridinium surfactants, RSC Adv. 6 (2016) 71692–71704.

[49] A. Neubrand, R. Lindner, P. Hoffmann, Room-temperature solubility behavior of barium titanate in aqueous media, J. Am. Ceram. Soc. 83 (2000) 860–864.

[50] K. Wenderich, G. Mul, Methods, mechanism, and applications of photodeposition in photocatalysis: a review, Chem. Rev. 116 (2016) 14587–14619.

[51] X. Li, C. Tang, Q. Zheng, Y. Shao, D. Li, Amorphous MoSx on CdS nanorods for highly efficient photocatalytic hydrogen evolution, J. Solid State Chem. 246 (2017) 230–236.

[52] R. Abe, K. Hara, K. Sayama, K. Domen, H. Arakawa, Steady hydrogen evolution from water on Eosin Y-fixed TiO$_2$ photocatalyst using a silane-coupling reagent under visible light irradiation, J. Photochem. Photobiol., A 137 (2000) 63–69.

[53] K. Kimura, T. Miwa, M. Imamura, The radiolysis and photolysis of methanolic solutions of eosin. I. The γ-radiolysis of neutral and alkaline solutions, Bull. Chem. Soc. Jpn. 43 (1970) 1329–1336.

[54] M.K. Gonce, E. Aslan, F. Ozel, I. Hatay Patir, Dye-Sensitized Cu2XSnS4 (X= Zn, Ni, Fe Co, and Mn) nanofibers for efficient photocatalytic hydrogen evolution, ChemSusChem 9 (2016) 600–605.

[55] F. Du, H. Lu, S. Lu, J. Wang, Y. Xiao, W. Xue, S. Cao, Photodeposition of amorphous MoSx cocatalyst on TiO2 nanosheets with 001 facets exposed for highly efficient photocatalytic hydrogen evolution, Int. J. Hydrogen Energy 43 (2018) 3223–3234.